9th International Colloquium on Bluff Body Aerodynamics and Applications
University of Birmingham, Birmingham, UK
29th July – 2nd August 2024

The influence of gantry rails on twin-box deck aerodynamics

Maja Rønne [a], Allan Larsen [b], Jens H. Walther [c], Tommaso Argentini [d], Daniele Rocchi [e]

[a] *COWI, Kgs. Lyngby, Denmark* mjre@cowi.com
[b] *COWI, Kgs. Lyngby, Denmark,* aln@cowi.com
[c] *Technical University of Denmark, Kgs. Lyngby, Denmark,* jhwa@dtu.dk
[d] *Politecnico di Milano, Milano, Italy,* Tommaso.argentini@polimi.it
[e] *Politecnico di Milano, Milano, Italy,* Daniele.rocchi@polimi.it

SUMMARY:
The present paper reports on wind tunnel tests and CFD simulations, carried out to investigate the effects of gantry rails on the aerodynamic performance of a twin-box bridge deck section. It is found that the aerodynamic performances, in terms of vortex induced vibration and flutter speed, of the analysed twin-box deck equipped with gantry rails is better than the similar girder without gantry rails. Specially the inner gantry rails close to the gap, have relevant effect on flutter stability and vortex induced vibrations. The inner gantry rails affect the flow upstream of the up-wind girder, reduce suction on the bottom surface of the cantilevered walkway, decreasing the contribution to negative moment coefficient, as compared to the girder without inner gantry rails. The increase in flutter stability is mainly due to the positive moment coefficient at zero angle of attack which induces nose-up rotation under wind action.

Keywords: Aerodynamic stability, Twin-box deck, Flutter, VIV, Wind tunnel tests, CFD

1. INTRODUCTION

Throughout the past decades, numerous experimental and numerical investigations on the aerodynamic performance of twin-box girders have been conducted, investigating the geometry of the twin girder hull, the width of the air gap and the influence of geometrical details such as wind screens and walkway porosity (Yang et al., 2015a,b; Argentini et al., 2022; Camera et al., 2023). Yang et al. (2015a,b) showed that an increase in central air gap (until a certain point) improves the flutter stability, as the aerodynamic torsional damping increases, but that the aeroelastic effects also are highly dependent on the shape of the girder. Kwok et al. (2012) observed that the lift force and pitching moment are more sensitive to the wind angle of attack than to the gap width. Further investigations of the gap width and effect of wind screens were conducted by Camera et al. (2023). Ogawa et al. (2002) found that the steady pitching moment characteristics, in terms of a positive moment at zero angle caused by a reduction of the negative pressure on the bottom of the leading side girder, and flutter stability for a twin-box girder, could be improved by attaching rails for an inspection cab to the bottom fairing and vertical plates to the lower flange of the girder.

In this work, the effects of gantry rails on the aerodynamic performance of a twin-box girder are studied in detail through investigation of the flutter stability and Vortex Induced Vibration (VIV). Static force coefficients from wind tunnel tests (WTT) and CFD simulations are examined. Furthermore, free motion tests, performed in the wind tunnel, are examined both for flutter instability and VIV.

2. INVESTIGATED DECK CONGIGURATIONS

Five variations of the twin-box deck of the 1915 Çanakkale Bridge are considered in this study, where the layout of the gantry rails changes. All five configurations have the same overall cross section geometry, see Figure 1. Configuration C1 includes all four gantry rails, both the outer ones and the inner ones close to the gap, configuration C2 is without gantry rails, configuration C9 includes the inner gantry rails only and configuration C10 includes only the outer gantry rails. Configuration C1A includes all four gantry rails, but the inner gantry rails are moved to the second position $0.017B$ inwards on the girder away from the gap, where B is the chord (deck) width, see Figure 1. Configuration C1A is only tested for vortex induced vibration (VIV) in the wind tunnel at the Boundary Layer Wind Tunnel Laboratory (BLWTL) at the University of Western Ontario, Canada through free vibration tests. The full-scale structural data for the different tested configurations are reported in Table 1.

2.1. Wind tunnel measurements

Wind tunnel tests have been conducted for the different configurations of the twin-box section of the 1915 Çanakkale Bridge. Static and free motion tests have been carried out for a $\lambda_L = 1:44$ geometrical scaled rigid section model in the (4m wide and 3.84m high) low turbulence test section of the wind tunnel at Politecnico di Milano (POLIMI). The section model used at POLIMI has a chord $B = 1.026\text{m}$ and a length $L = 3.84\text{m}$, with aspect ratio $L/B = 3.74$. To measure the model rotation, the model was equipped with an inclinometer at the transverse cross beam of the model at end span section. Furthermore, the model was equipped with two pairs of accelerometers, one pair at half span section and one pair at end span section, on the leading and trailing edges. The rotation and vertical displacement of the deck model were measured by means of two laser transducers placed at mid-span on the wind tunnel floor pointing on the lower surface of the two girders. All tests at POLIMI were conducted in smooth flow conditions with turbulence intensity $I_u < 0.1\%$ and at Reynolds numbers in the order of $\text{Re} = \frac{\rho UB}{\mu} \simeq 10^6$, where ρ is the air density, U is the mean wind speed and μ is the dynamic viscosity.

Wind tunnel tests of the VIV response of the configuration C1, C1A and C2 have been carried out on a $\lambda_L = 1:30$ scaled section model in the low-speed test section (4.88m wide and 3.66m high) of the BLWTL. This model has a chord $B = 1.50\text{m}$ and a length of $L = 3.66\text{m}$, with aspect ratio $L/B = 2.44$. The model was tested in a unique, custom-made dynamic test rig, suspended by springs, and restrict to vertical displacement only, by a parallel motion mechanism consisting of two leaf-springs at each end of the model. Four laser transducers, two at each end of the model, were used to measure the vertical and torsional motion. Additional four accelerometers were placed on the model, one at each end and one pair at the midspan of the section model on each deck hulls. The tests were conducted in smooth flow conditions $(I_u < 1.0\%)$ at Reynolds numbers in the order of 5×10^5.

2.2. CFD simulations

For obtaining a better understanding of the influence of the gantry rails on the flow around the twin-box girder, CFD simulations are conducted for the four configuration C1, C2, C9 and C10 of the 1915 Çanakkale Bridge. The CFD simulations are performed in the time domain for stationary sections using the STAR-CCM+ software version 18.06.006, employing a 3D URANS model with the SST k-ω turbulence model. Preliminary 2D simulations did not give satisfactory results, in particular for the moment coefficient. Implicit unsteady, segregated flow of second order is used

with a non-dimensional time step of $\Delta tU/B = 0.001$ and 10 inner iterations. Smooth flow condition has been adopted, with a turbulence intensity of $I_u = 1.0\%$ set at the domain inlet, and a turbulent viscosity ratio of 10. The Reynolds number of the CFD simulations is $\mathrm{Re} = 10^6$.

The dimensions of the fluid domain for the simulations are $11B$ in the stream-wise direction, with $3B$ in front of the bridge girder, $4B$ in the cross-wind vertical direction and $0.53B$ in the transverse direction (along the bridge axis). The depth of the domain, $0.53B$, includes one cross beam and is defined in order to have planes with periodic interfaces. The boundary condition for the plane of the fluid domain behind the bridge girder is defined as pressure outlet, and the planes in front of the girder, above and below of the girder are set as velocity inlet. Wall boundary conditions are chosen for all the parts of the bridge girder. A polyhedral mesh is used for the fluid domain with prism layer mesh consisting of ten rows at the surface of the bridge girder. The simulations contain up to $23.6\text{x}10^6$ cells. An "all y^+ wall treatment" model is adopted, which combines the high y^+ wall treatment for coarse meshes and the low y^+ wall treatment for fine meshes. This treatment resolves the boundary layer up to the wall and assumes that the near-wall cell lies within the logarithmic region of the boundary layer and that the viscous sublayer is well resolved by the mesh. In general, the maximum wall y^+ value for the simulations is below 1.25 with a few high values at the up-wind wind screens and up-wind crash barrier.

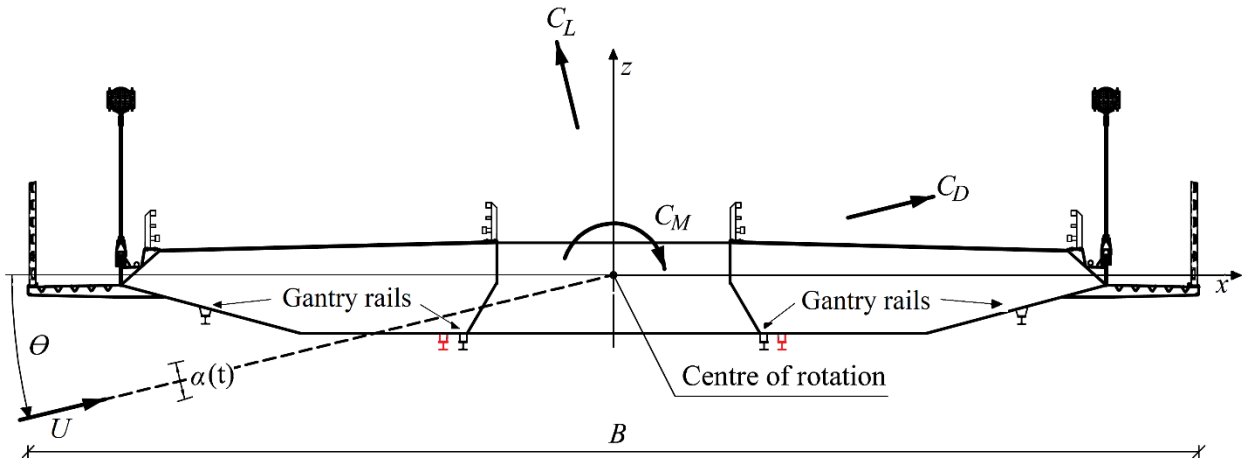

Figure 1. Geometry of the tested twin-box girder section with gantry rails on and the definition of the sign convention for the static force coefficients. In red: secondary position of gantry rails for configuration C1A.

Table 1 Full-scale structural data for the tested twin-box deck section for the different configurations.

Configuration	Mass m [kg/m]	Mass moment of inertia I [kg · m^2/m]	Vertical frequency f_z [Hz]	Torsional frequency f_α [Hz]
C1 & C1A	28853	6.215×10^6	0.072	0.146
C2	28293	6.136×10^6	0.073	0.147
C9	28573	6.145×10^6	0.072	0.147
C10	28573	6.205×10^6	0.072	0.146

3. STATIC FORCE COEFFICIENTS AND FLOW

The static force coefficients for the drag, lift and moment for the twin-box deck section at POLIMI were measured in the static test rig. The model was equipped with two external 6-componant force balances. Electrical controlled actuators connected to the model allows it to be rotated around the bridge axis to change the wind angle of attack. The measurement of the static force coefficients was repeated for wind speed values ranging between 5 and 20m/s, to verify their Reynolds number independency.

From the CFD simulations, the static, time averaged, wind load coefficients, are extracted from the time series, when the signal has stabilized. Furthermore, the mean flow field and mean pressure distribution on the girder are evaluated when the signals for the static force coefficients have stabilized. The static force coefficients C_D, C_L and C_M from the WTT at POLIMI and CFD simulations are shown in Figure 2 as function of the angle of attack θ. The static force coefficients are defined as:

$$C_D = \frac{D}{\frac{1}{2}\rho U^2 B} \quad , \quad C_L = \frac{L}{\frac{1}{2}\rho U^2 B} \quad , \quad C_M = \frac{M}{\frac{1}{2}\rho U^2 B^2} \tag{1}$$

where D, L and M are the drag, lift and moment per unit length, with the sign convention as shown in Figure 1 (moment and angle of attack positive nose-up, lift positive upwards).

From Figure 2 a good agreement is seen between the CFD simulations and WTT for the lift and moment coefficient. The drag coefficient in the CFD simulations for a given configuration is generally lower compared to the wind tunnel tests for the same configuration but have the overall same trend. It is noted from Figure 2, that the drag, lift, and moment coefficients all are lower for the configurations without inner gantry rails (C2 and C10), compared to the section with the inner gantry rails (C1 and C9). Furthermore, the coefficients for the configuration with both outer and inner gantry rails (C1) and the configuration with only inner gantry rails (C9) are almost identical. Also, the coefficients for the configuration without any gantry rails (C2) and the configuration with only outer gantry rails (C10) are similar. This suggests that the inner gantry rails play a critical role as they have the greatest impact on the flow and corresponding coefficients. In Figure 2 some deviations are seen in the CFD simulations of configuration C9 for drag, lift, and moment coefficient and for configuration C2 for the drag and lift coefficient at $\theta = 3°$ angle of attack. For zero angle of attack, a positive moment coefficient is observed for the sections with inner gantry rails (C1 and C9) whereas a negative moment coefficient is seen for the sections without inner gantry rails (C2 and C10). This will make the elastically supported sections of configuration C1 and C9 rotate nose-up and configuration C2 and C10 rotate nose-down under high wind loading. The slope of the moment coefficient curves is positive for all configurations for angles of attack larger than $-3°$, and (generally) decreases for increasing angles of attack. A slightly increase in the moment slope is noted for configuration C2 from $-1°$ to $1.5°$ angle of attack. A positive moment coefficient at zero angle of attack, and a positive slope, decreasing with increasing angles of attack, ensures that the elastically supported deck will rotate nose-up keeping stability performances according to Quasi Steady Theory (QST) (Rønne et al., 2024; Larsen and Sørensen, 2022). In the QST the development of the angle of attack θ as function of the mean wind speed

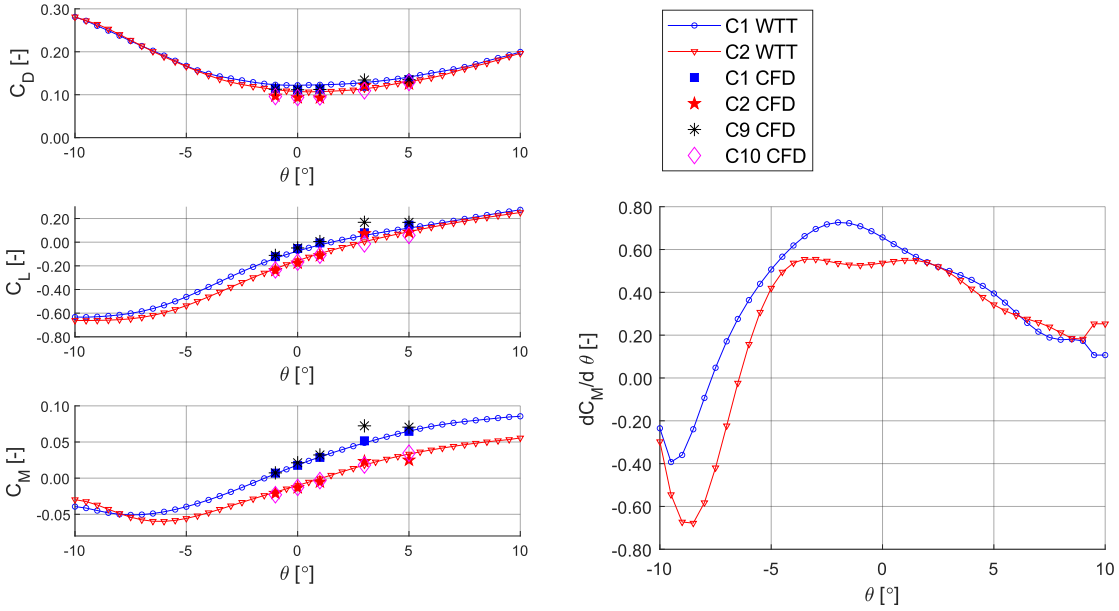

Figure 2. Static force coefficients C_D, C_L, C_M, and moment slope $dC_M/d\theta$, as function of the angle of attack θ, for the four section configurations C1 (with gantry rails on), C2 (without gantry rails), C9 (with inner gantry rails) and C10 (with outer gantry rails) from the WTT and CFD.

U is evaluated by assuming that the aerodynamic moment is balanced by the moment capacity of the elastically suspended section, cf. Eq. (2). Furthermore, the QST expresses a simplified formular for the critical flutter wind speed U_{crit} as given in Eq. (3).

$$I(2\pi f_\alpha)^2\theta = \frac{1}{2}\rho U^2 B^2 (C_{M2}\theta^2 + C_{M1}\theta + C_{M0}) \tag{2}$$

$$U_{crit} = 2\pi f_\alpha B \sqrt{\frac{I\left(1-\left(\frac{f_z}{f_\alpha}\right)^2\right)}{\rho B^4 \frac{dC_M}{d\theta}\mathcal{F}}} \tag{3}$$

In Eq. (2) $I(2\pi f_\alpha)^2$ is the torsional static stiffness of the system, C_{M2}, C_{M1} and C_{M0} are the parameter values for a 2nd order parabolic curve fit to the moment coefficient. In Eq. (3) the empirical factor $\mathcal{F}$ applied to the moment slope $dC_M/d\theta$ serves the same purpose as the real part of Theodorsen circulation function in the "flat plate" aerodynamics. The purpose of the $\mathcal{F}$ factor is to model the depreciation of the aerodynamic moment caused by the oscillatory wake of the deck. Eq. (3) describes increasing critical wind speed proportional to the torsional frequency, the square root of the mass moment of inertia and the square root of decreasing moment slope $dC_M/d\theta$. The slope of the moment should be at the static angle of attack where flutter instability is expected. The static angle of attack and the critical flutter wind speed is found through an iterative prosses, using Eq. (2) and Eq. (3). The critical wind speed from Eq. (3) for a given static angle of attach, is inserted in Eq. (2), and a new static angle of attack is obtained, which again is

used in Eq. (3) for defining the moment slope. Due to the development of the moment curve, cf. Figure 2, configuration C2 rotate nose-down and the critical wind speed for onset of flutter stabilize around $64.7\mathrm{m/s}$ at a rotation angle of $-1.2°$. Configuration C1 rotate nose-up, and the critical wind speed for onset of flutter continue increasing for increasing angles of attack. This coincides with the findings from the free motion tests in section 4.

From the mean flow field around the girders of the different configurations, Figure 3, a larger flow velocity is observed at the lower side of the up-wind (UW) cantilevered walkway for the sections without inner gantry rails, C2 and C10. This larger velocity is resulting in a higher suction on the bottom surface of the up-wind girder, see Figure 4, and is the reason for the negative moment coefficient at zero angle of attack cf. Figure 2. The inner gantry rails affect the flow in the gap, increasing the mass flow through the gap by around 22-33%, which influences the flow upstream of the UW girder and the flow around the down-wind (DW) girder, creating a larger area with low

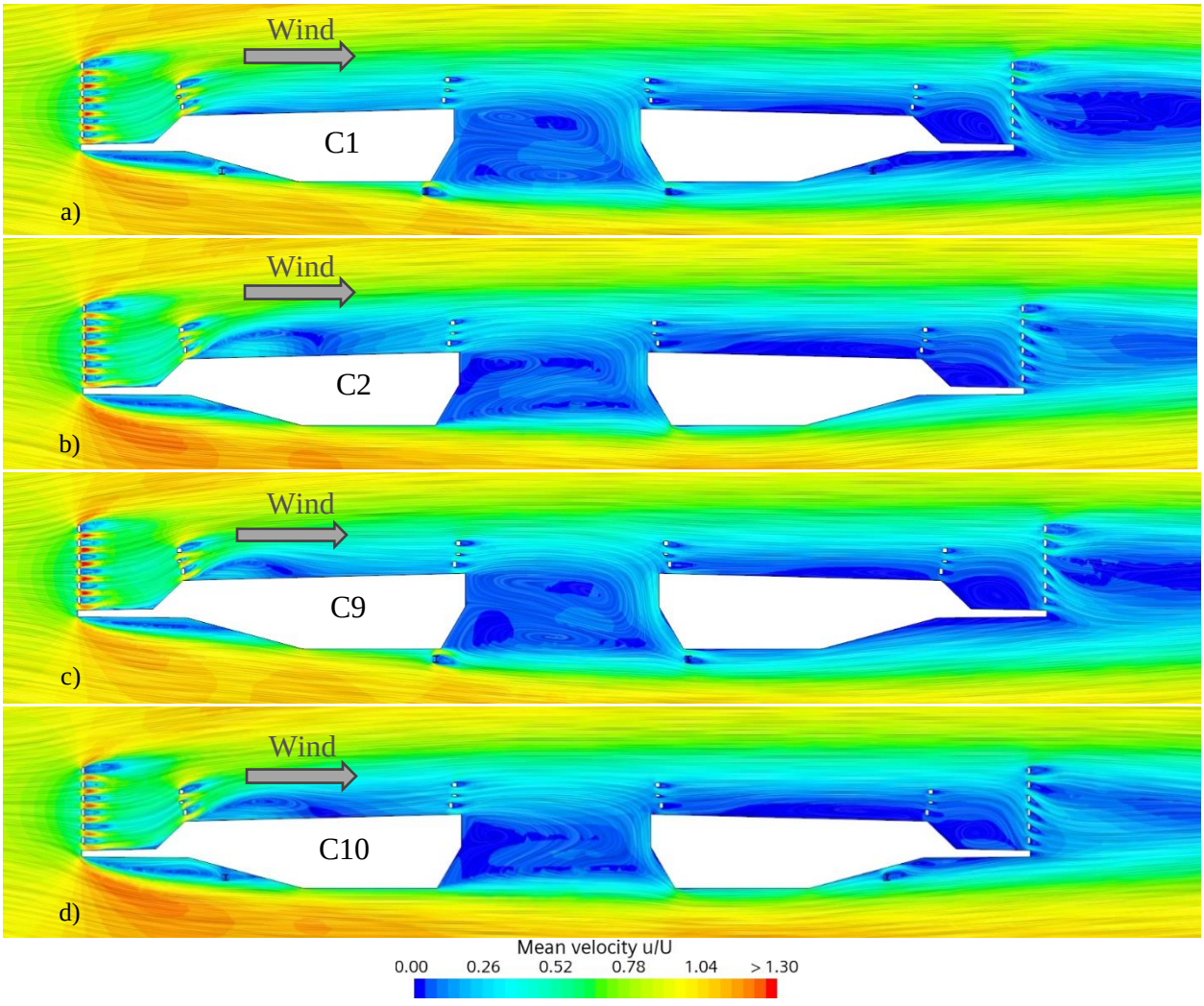

Figure 3 Flow visualization of the mean velocity around the cross section for the different configurations of the CFD simulations. a) configuration C1 with gantry rails on, b) C2 without gantry rails, c) C9 with inner gantry rails and d) C10 with outer gantry rails.

velocity at the bottom surface of the DW girder. For the configurations with inner gantry rails (C1 and C9), cf. Figure 3, the vortices in the gap are higher, compared to configuration C2 and C10, where the vortices in the gap are slimmer.

In Figure 3, flow separation on the top of the UW girder is observed for configuration C2, C9 and C10. For configuration C1 no separation is observed. It seems like including both the inner and outer gantry rails on the girder (configuration C1), creates some asymmetry in the flow on both side of the cross beam, both in the gap and on the top of the girder. This asymmetry causes a higher turbulence on the top surface of the UW girder, which give a trip wire effect that attaches the flow to the girder surface, resulting in no flow separation.

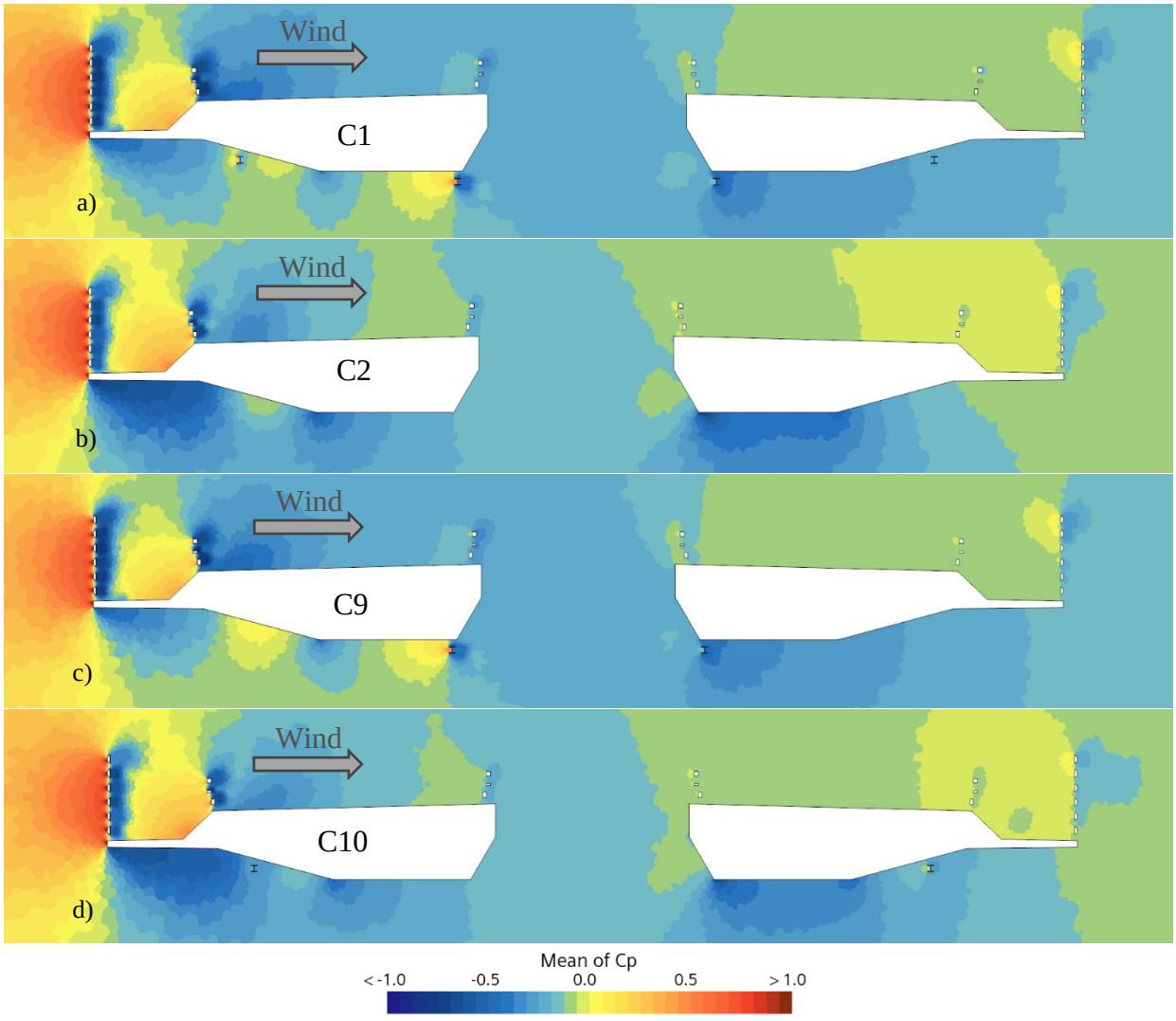

Figure 4 Pressure distribution around the up-wind (UW) and down-wind (DW) girder of the cross section for the configuration of the CFD simulations. a) configuration C1 with gantry rails on, b) C2 without gantry rails, c) C9 with inner gantry rails and d) C10 with outer gantry rails.

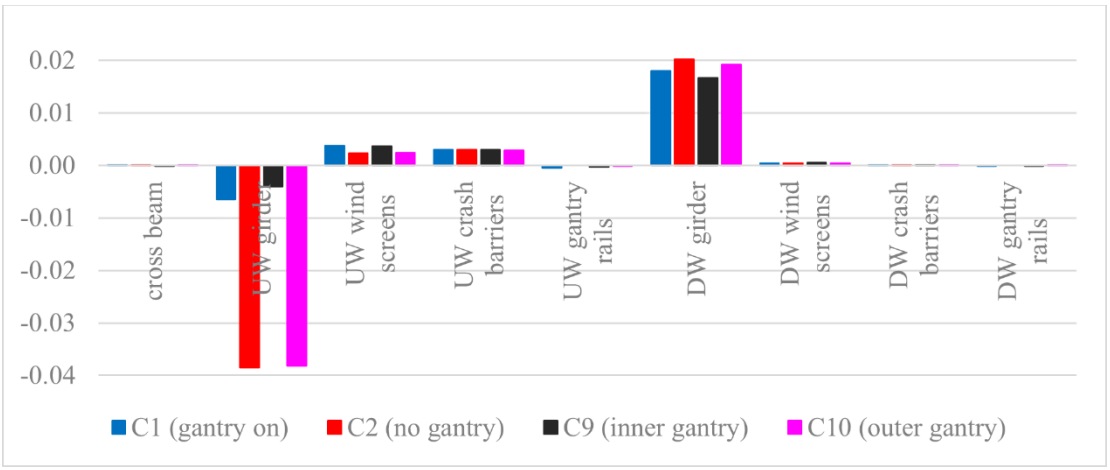

Figure 5 The contribution to the moment coefficient from the different bridge elements for configuration C1, C2, C9 and C10 for $\theta = 0°$ angle of attack.

The CFD pressure distributions around the girders of the different configurations are shown in Figure 4 and the contribution to the moment coefficient from the pressure of the different girder elements are summarised in Figure 5. In Figure 4, the pressure distributions are shown as the mean pressure coefficient $C_P = \frac{\Delta P}{\frac{1}{2}\rho U^2}$, where ΔP is the change in the absolute pressure. It is noted from Figure 5 that it is not the moment contribution of the gantry rails itself, but the change in the flow field and thereby the pressure distribution, cf. Figure 4, specially for the UW girder that makes the difference in the overall moment coefficient and thereby the stability. The change in the moment coefficient is mainly due to the change in the pressure at the bottom surface of the UW girder and especially at the bottom surface of the cantilevered walkway.

4. CRITICAL FLUTTER WIND SPEED

For the free motion tests at POLIMI, the model of the different configurations was elastically suspended on springs, prevented to move in the horizontal direction, but free to move in the vertical $z(t)$ and torsional $\alpha(t)$ motion. The horizontal motion was constrained by two parallel steel bars at each end of the model, connected to model by bearings and fixed to the wall of the wind tunnel by vertical bars. The free motion tests procedure consisted of forcing the model to oscillate in the torsional mode, which is aero-elastically coupled with the vertical mode at instability. For each test, the dynamic responses were recorded after the model was released for the forced motion. The process was repeated for a range of increasing wind speeds, until instability was reached. For the tests close to the critical wind speed for onset of flutter, the model was simply released from a fixed position and no additional force was put into the motion.

The flutter wind speed and corresponding static rotation of the elastically suspended model of the girder configurations C1, C2 and C9 are shown in Figure 6. Configuration C10 has not yet been tested in the wind tunnel. The girder configuration C1, with both inner and outer gantry rails, and the girder C9, with only inner gantry rails, were both stable and did not reach flutter instability. Configuration C1 was testes up to a full-scale wind speed at the maximum $91\mathrm{m/s}$. A rotation angle of $8.2°$ was recorded for this velocity. For configuration C9 flutter was not reached at a full-

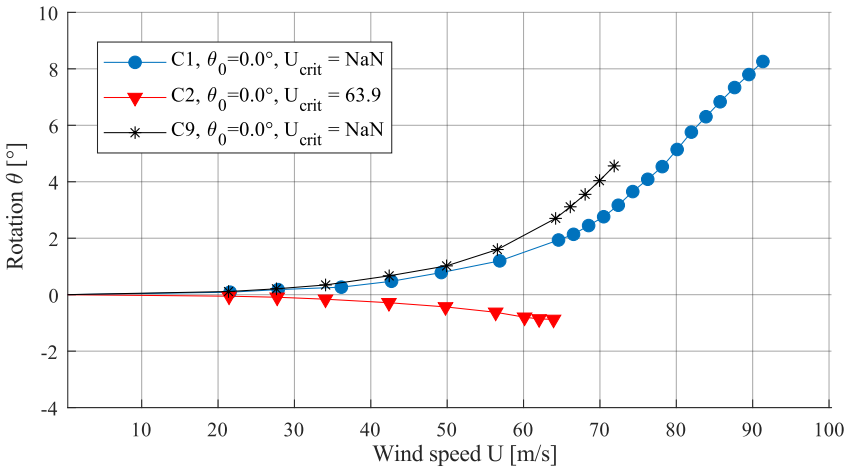

Figure 6 Critical wind speed tests of configuration C1, C2 and C9 from the wind tunnel tests at POLIMI. The figure shows the reached equilibrium for the angle of attack as function of the mean wind speed.

scale wind speed of 72m/s, where a rotation angle of $4.6°$ was observed. Configuration C2 without any gantry rails reaches the onset of flutter at a full-scale wind speed of 64m/s and with a rotation angle of $-0.9°$. Configuration C2, has a negative moment coefficient at zero angle of attack, cf. Figure 2, making the elastically suspended cross section rotate nose-down, compared to the configurations with inner gantry rails (C1 and C9), which have a positive moment coefficient at zero angle of attack making the elastically suspended model rotate nose-up.

5. VIV RESPONSE

The vertical RMS response of the VIV from the wind tunnel tests conducted at BLWTL is shown in Figure 7. The tests were performed in smooth flow, for a range of increasing wind speeds, recording 60s of the resulting vertical motion time history.

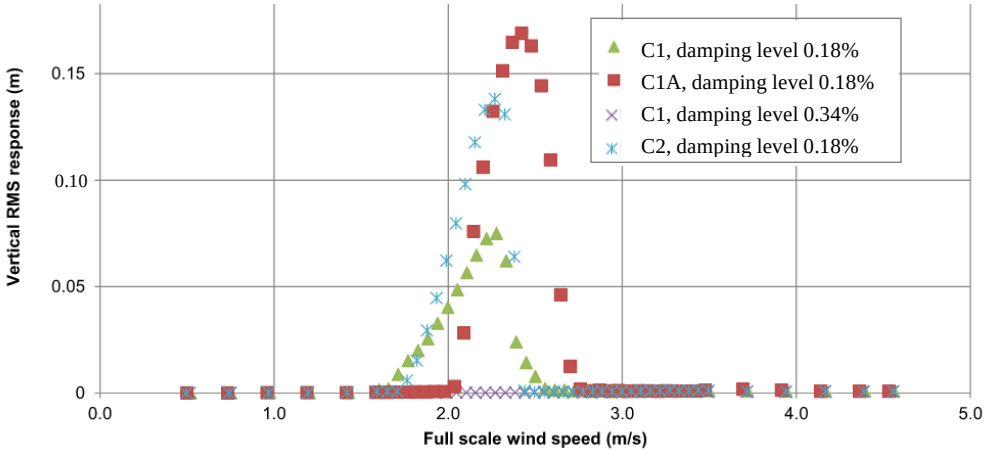

Figure 7. The RMS lift responses for different test conditions (C1, C2 and C1A), for $\theta = 0°$ angle of attack, from the WTT at BLWTL. Configuration C1 is tested for two structural damping ratios, 0.18% and 0.34%.

From Figure 7 it is noted that the VIV response for configuration C1 with both outer and inner gantry rails at originally position, see Figure 1, is smaller than for the configuration C2 without gantry rails, for the same damping level, 0.18% rel.-to-crit. However, moving the inner gantry rails $0.017B$ (0.75m full-scale) inwards on the girder, to the second position, configuration C1A, results in larger RMS responses than configuration C2 without gantry rails. Thus, the position of the gantry rails has an important role in the twin-box girder stability. By increasing the damping level to 0.34% rel.-to-crit. for configuration C1, no vortex induced vibration is observed.

6. CONCLUSIONS

Details such as gantry rails are important for the design of twin-box girders. In the present study, especially the inner gantry rails have proved to be critical for the flutter stability and vortex induced vibration of the twin-box girder. Including the inner gantry rails are generally more important for the stability both in terms of critical wind speed for onset of flutter and response of VIV. Also, the exact position of the gantry rails is important and affects the VIV response. Moving the inner gantry rails inwards along the girder bottom plate, to a secondary position, results in larger VIV response than observed for the girder without gantry rails. Including the inner gantry rails on the twin-box girder, results in a positive moment coefficient at zero angle of attack, and a positive slope, decreasing with increasing angles of attack, ensuring that the elastically supported deck will rotate with nose-up. The inner gantry rails affect the flow in the gap, which influence the flow upstream of the up-wind girder and affect the pressure distribution on the bottom surface of the cantilever walkway and top surface of the girder.

ACKNOWLEDGEMENTS

Thanks to the skilled people at POLIMI (including Umberto Spinelli, Frederico Zanelli, Nicola Cortellazzi, Frederico Di Lenardo, Luca Ronchi, Stefano Giappino and Alessandro Brambilla, among others) and BLWTL (L. Kong, T. G. Mara and J. P. C. King) for making the wind tunnel tests.

REFERENCES

Argentini, T., Rocchi, D., Somaschini, C., Spinelli, U., Zanelli, F. and Larsen, A., 2022. Aeroelastic stability of a twin-box deck: Comparision of different procedures to assess the effect of geometric details. J. Wind Eng. Ind. Aerodyn. 220, 104878. doi:10.1016/j.jweia.2021.104878.

Camera, A., Bagnara, A., Larsen, A., Cammelli, S. and Piccardo, G., 2023. The effect of central gap and wind screens on the aeroelastic stability of long-span bridge decks: Comparison of numerical analyses and experimental results. J. Fluid. Structs.121, 103923. doi:10.1016/j.jfluidstructs.2023.103923.

Kwok, K. C. S., Qin, X. R., Fok, C. H. and Hitchcock, P. A., 2012. Wind-induced pressures around a sectional twin-deck bridge model: Effects on gap-width on the aerodynamic forces and vortex shedding mechanisms. J. Wind Eng. Ind. Aerodyn., 110, 50-61. doi:10.1016/j.jweia.2012.07.010.

Larsen, A. and Sørensen, J. W. 2022. Benefits and Challenges of the Twin-box Bridge Girder. IABSE Congress, Nanjing, China.

Ogawa, K., Shimodoi, H. and Oryu, T., 2002, Aerodynamic characteristics of a 2-box grider section adaptable for a super-long span suspension bridge. J. Wind Eng. Ind. Aerodyn., 90, 2033-2043.

Rønne, M., Larsen, A., Walther, J. H. and Larsen, S. V., 2024, Flutter stability of twin-box bridge decks. Submitted to Proceedings of the ICWE16 Conference, published by Springer Nature.

Yang, Y., Wu, T., Ge, Y. and Kareem, A., 2015a, Aerodynamic stabilization mechanism of a twin box girder with various slot widths. J. Bridge Eng., 20, 04014067, doi:10.1016/(ASCE)BE.1943-5592.0000645.

Yang, Y., Zhou, R., Ge, Y., Mohotti, D. and Mendis, P., 2015b, Aerodynamic instability performance of twin box girders for long-span bridges, J. Wind Eng. Ind. Aerodyn., 145, 196-208. doi:10.1016/j.jweia.2015.06.014.